

1 Quantifying Temperature-sliding Inconsistency in Thermomechanical Coupling: A
2 Comparative Analysis of Geothermal Heat Flux Datasets at Totten Glacier

3
4 Junshun Wang¹, Liyun Zhao¹, Michael Wolovick², John C. Moore³

5 ¹State Key Laboratory of Earth Surface Processes and Hazards Risk Governance
6 (ESPHR), Faculty of Geographical Science, Beijing Normal University, Beijing
7 100875, China

8 ²Glaciology Section, Alfred-Wegener-Institut, Helmholtz-Zentrum für Polar- und
9 Meeresforschung, Bremerhaven, Germany

10 ³Arctic Centre, University of Lapland, Rovaniemi, Finland

11 *Correspondence: Liyun Zhao (zhaoliyun@bnu.edu.cn), John C. Moore*
12 *(john.moore.bnu@gmail.com)*

13
14
15
16 **Abstract.** Rapid sliding of ice sheets requires warm basal temperatures and lubricating
17 basal meltwater, whereas slow velocities typically correlate with a frozen bed. However,
18 ice sheet models often infer basal sliding by inverting surface velocity observations
19 with the vertical structure of temperature and hence rheology held constant. If the
20 inversion is allowed to freely vary sliding over the model domain, then inconsistencies
21 between the basal thermal state and ice motion can arise lowering simulation realism.
22 In this study, we propose a new method that quantifies inconsistencies when inferring
23 thawed and frozen-bedded regions of ice sheets. This method can be used to evaluate
24 the quality of ice sheet simulation results without requiring any englacial or subglacial
25 measurements. We apply the method to evaluate simulation results for Totten Glacier
26 using an isotropic 3D full-Stokes ice sheet model with eight geothermal heat flux (GHF)
27 datasets and compare our evaluation results with inferences on basal thermal state from
28 radar specularity. The rankings of GHF datasets based on inconsistency are closely
29 aligned with those using the independent specularity content data. Examples of the
30 method utility are 1. an overcooling inconsistency with all GHFs near the western
31 boundary of Totten Glacier between 70°S-72°S, where there is a bedrock canyon and
32 fast surface ice velocities, suggesting that all GHFs are low; 2. an overheating
33 inconsistency in the eastern Totten Glacier with all GHFs suggesting overestimation of
34 ice temperature due, in this case, to an unrealistically warm surface temperature. Our
35 approach opens a new avenue for assessing the self-consistency and reliability of ice
36 sheet model results and GHF datasets, which may be widely applicable.

38 **1. Introduction**

39 Ice sheet models are an important tool for projections of ice sheet mass balance
40 and their contribution to sea level rise. Ice sheet models are usually initialized by “spin-
41 up” or data assimilation such that they reproduce the present-day geometry or surface
42 velocity of an ice sheet (Seroussi et al., 2019). Often ice sheet model simulations derive
43 ice dynamics using ice temperatures taken from other studies (e.g., Gillet-Chaulet et al.,
44 2012; Van Liefferinge and Pattyn, 2013; Cornford et al., 2015; Pittard et al., 2016;
45 Siahhaan et al., 2022). In thermo-mechanically coupled ice sheet simulations, the ice
46 sheet model is usually spun up with idealized temperature-depth profiles and then run
47 in a thermo-mechanically coupled mode constrained by geothermal heat flux (GHF)
48 and surface ice temperature fields (Seroussi et al., 2019). While advances in satellite
49 and field observation technologies have led to a preliminary consensus on ice sheet
50 geometry and surface ice temperature, significant uncertainties persist in basal
51 boundary conditions, including GHF and basal friction, since reliable observational
52 data are scarce. These basal properties introduce significant uncertainty in the simulated
53 ice sheet dynamics, and thus ice sheet mass balance.

54 The GHF, the heat flow from the Earth's crust to the base of ice sheet, is a critical
55 variable in the basal boundary condition for simulating the ice temperature profile, and
56 hence ice rheology and flow dynamics (Fisher et al., 2015; Smith - Johnsen et al., 2020;
57 Reading et al., 2022). Several GHF datasets exist, derived in various ways from
58 geophysical observations and models, and they exhibit significant variability in both
59 spatial distribution and magnitude (e.g., An et al., 2015; Dziadek et al., 2017; Martos et
60 al., 2017; Shen et al., 2020; Stål et al., 2021). These GHF datasets have been widely
61 used in thermodynamic simulations of Antarctica (e.g., McCormack et al., 2022;
62 Shackleton et al., 2023; Park et al., 2024; Van Liefferinge et al., 2018). However,
63 assessing the GHF field accuracy is problematic because in situ measurements such as
64 boreholes are sparse. Few studies have assessed the quality and reliability of GHF
65 datasets over specific regions. Kang et al. (2022) employed a combination of forward
66 model and inversion using a 3D full-Stokes ice flow model to simulate the basal thermal
67 state in the Lambert–Amery Glacier region and evaluate different GHFs using the
68 locations of subglacial lakes, but the constraints used were asymmetric between frozen
69 and thawed beds, and assigned inflated reliability to the warmer GHF maps. Indirect
70 estimates of basal conditions have used airborne radar specularity content (Schroeder
71 et al., 2013, 2015; Young et al., 2016) as proxies for basal wetness/dryness and thermal
72 regime (Dow et al., 2020). Huang et al. (2024) used an inverse modeling approach
73 similar to that of Kang et al. (2022) for Totten Glacier and combined this with measured
74 radar specularity content to derive a two-sided constraint on the basal thermal state in
75 addition to subglacial lakes locations. However, specularity content is not yet available
76 for many regions of Antarctica.

77 The basal friction field is another poorly known boundary condition in ice sheet
78 modeling, and a key source of uncertainty in the long-term projection of ice sheets and
79 glaciers. Although basal slip is crucial to the 3D ice flow, it is difficult to observe.
80 Several basal sliding parameterizations have been proposed and widely used
81 (Weertman, 1957; Kamb, 1970; Nye, 1970; Budd et al., 1979; Fowler, 1981; Schoof,
82 2005; Gagliardini et al., 2007; Gladstone et al., 2014; Tsai et al., 2015; Brondex et al.,
83 2017, 2019). The linear Weertman basal sliding parameterization is the most widely
84 used due to its simple form. Given prescribed or modelled ice temperatures and hence
85 ice viscosity, numerous studies have inferred the spatial distribution of basal friction
86 coefficient over grounded ice to best match observed present-day surface ice velocities
87 or ice sheet geometry using snapshot or time-dependent data assimilation and inverse
88 methods (MacAyeal, 1993; Morlighem et al., 2010; Rignot et al., 2011; Gillet-Chaulet
89 et al., 2012; Larour et al., 2012; Pollard and DeConto, 2012; Morlighem et al., 2013;
90 Perego et al., 2014; Pattyn, 2017; Albrecht et al., 2020; Lipscomb et al., 2021; Choi et
91 al., 2023). However, such inversions typically allow the friction coefficient to vary
92 freely to match the surface velocity observations. This can potentially lead to conflicts
93 with the temperature field used during the inversion, which we refer to as
94 “inconsistencies” in this study. For instance, relatively fast surface ice velocity may
95 demand basal sliding in areas where the basal temperatures are below the local pressure
96 melting point. These inconsistencies may be due to unrealistic ice temperatures or a
97 lack of complete physics in the ice sheet model. However, many studies overlook this
98 aspect, and use the inversion results to initialize ice sheet dynamics simulations and
99 estimate glacier mass balance and its contribution to sea level rise (Seroussi et al., 2019;
100 Peyaud et al., 2020; Schannwell et al., 2020; Payne et al., 2021).

101 To the best of our knowledge, there has been no study of such inconsistencies
102 between a sliding inversion and the temperature/rheology field used as an input to that
103 inversion. Here we develop a novel and generally applicable method to estimate this
104 inconsistency without relying on basal observation data. We utilize the inconsistency
105 of the modelled ice temperature and observed velocity fields to evaluate the quality of
106 ice flow model results. Notably, this approach can also serve as a supplementary method
107 for assessing geothermal heat flux datasets, relying solely on surface ice velocity
108 observations rather than additional englacial or subglacial data.

109 We apply our method to Totten Glacier, a primary outlet of the Aurora subglacial
110 basin in East Antarctica (Greenbaum et al., 2015; Pritchard et al., 2009). The Totten
111 Glacier subregion experienced the largest mass loss among drainage basins in East
112 Antarctica during the period 1979-2017 and 2003-2020 (Kim et al., 2024; Rignot et al.,
113 2019) (Fig. 1a). We examine inconsistencies between simulated ice temperature and ice
114 velocity fields using a 3D full-Stokes model using the various GHFs included in Huang
115 et al. (2024) and use this analysis to rank the reliability of different GHF fields. This

116 GHF ranking closely resembles that reported by Huang et al. (2024), which used the
117 agreement between the modelled basal thermal regime and specular content, which
118 we take as a validation of the method. Since the new method does not require any
119 englacial or subglacial data, it can be applied to many glaciers, particularly those
120 lacking observations. Our approach can provide a swift assessment of the plausibility
121 of basal temperature and velocity simulated by ice sheet models. Additionally, it can be
122 effectively utilized to map the spatial distribution of GHF over- or under-estimation.

123

124 **2. Method**

125 **2.1 Methodology in this study**

126 The inconsistencies defined in this study are essentially between a sliding
127 inversion and the temperature/rheology field used as an input to that inversion. More
128 specifically, the inconsistencies are between modelled basal sliding (which is tuned to
129 match the observed fast surface velocity during the inversion) and modelled frozen bed,
130 and between observed slow surface velocity (which is most likely indicative of a non-
131 slip basal condition) and modelled thawed bed. The inconsistencies originate from
132 multiple causes, including uncertainties in GHF, surface ice temperature, ice sheet
133 geometry, bed topography, surface velocity, ice density and incomplete ice flow
134 mechanics.

135 There is no direct correlation between basal temperature and surface velocity;
136 rather, they are linked through the basal thermal state - the basal temperature being at
137 or below the pressure melting point. The ice bottom in the study domain can be
138 partitioned into thawed and frozen beds depending on whether the simulated basal ice
139 temperature reaches the local pressure melting point. To effectively penalize models
140 exhibiting both localized overheating (bed too warm) and overcooling (bed too cold),
141 we establish overheating metrics within the thawed-bedded region and overcooling
142 metrics within the frozen-bedded region to quantitatively assess the inconsistency
143 between the simulated temperature and velocity fields. Thus, we provide two-sided
144 constraints on the temperature field that penalize both too high and too low ice
145 temperature.

146 Overcooling occurs where basal temperature is underestimated. Crucially, in
147 regions with relatively fast observed surface velocity, the inverse method nevertheless
148 yields a nonzero basal velocity — a physically inconsistent result given the cold basal
149 temperature. When basal ice temperature is below the pressure melting point, the basal
150 modelled velocity is expected to approach zero. This inconsistency is larger for faster
151 simulated basal ice speed and for colder simulated basal temperatures. We therefore use
152 a formula that accounts for both variables to quantify overcooling:

$$153 \quad AOC = (T_{melt} - T_{bm}) \times U_{bm}, \quad (1)$$

154 where AOC stands for absolute overcooling, T_{melt} is the basal pressure melting point,

155 T_{bm} represents the simulated basal ice temperature and U_{bm} means the simulated basal
 156 ice speed.

157 For the overheating metric, since the first term of the right-hand side of Eq. (1)
 158 becomes zero at a thawed bed, we cannot use a similar formula as Eq. (1). It is not
 159 straightforward to quantify the inconsistencies between modelled thawed bed and
 160 expected slow basal speed given slow observed surface speed. We note the fact that
 161 modelled basal sliding speed must remain non-negative. If the ice is warm and soft
 162 enough to permit deformation such that the modelled surface speed is much faster than
 163 the observed, then a friction inversion will be ineffective to correct this misfit,
 164 producing a bias towards positive misfits (i.e., model velocities are too fast) in the
 165 inversion results. Therefore, we use the positive difference between the simulated
 166 surface ice speed and the observed speed to calculate the inconsistency caused by the
 167 overheating effect:

$$168 \quad AOH = \max(0, U_{sm} - U_{obs}), \quad (2)$$

169 where AOH refers to absolute overheating, U_{sm} represents the modelled surface ice
 170 speed and U_{obs} is the observed surface ice speed. We only calculated AOH for the
 171 thawed-bedded areas, i.e. $T_{bm} = T_{melt}$, because observed surface ice speed errors are
 172 proportionally much less in thawed-bedded areas (corresponding to fast flow regions)
 173 than in frozen-bedded area (correspond to slow flow regions).

174 To mitigate the impact of substantial differences in observed surface ice speed
 175 across various areas, we also define "relative overheating" (ROH) and "relative
 176 overcooling" (ROC), dividing AOH and AOC by the observed surface ice speed
 177 respectively:

$$178 \quad ROH = \frac{\max(0, U_{sm} - U_{obs})}{U_{obs}}, \quad (3)$$

$$179 \quad ROC = (T_{melt} - T_{bm}) \times \frac{U_{bm}}{U_{obs}}. \quad (4)$$

180 Overheating and overcooling inconsistencies are calculated on thawed bed and
 181 frozen bed, respectively. To evaluate the inconsistencies for the whole domain, we
 182 linearly normalized the overheating inconsistency and overcooling inconsistency to
 183 range from 0 to 1 and then sum them as:

$$184 \quad ACI = L_N(AOC) + L_N(AOH), \quad (5)$$

$$185 \quad RCI = L_N(ROC) + L_N(ROH), \quad (6)$$

186 where ACI means absolute combined inconsistency, RCI represents relative combined
 187 inconsistency, and L_N represents linear normalization. Taking AOC as an example, its
 188 linear normalization is:

$$189 \quad L_N(AOC) = \frac{AOC - AOC_{min}}{AOC_{max} - AOC_{min}}. \quad (7)$$

190 Therefore, we obtain 6 metrics consisting of three absolute inconsistencies (AOH , AOC ,

191 *ACI*) and three relative inconsistencies (*ROH*, *ROC*, *RCI*).

192 These 6 indicators can comprehensively analyze the temperature-sliding
193 inconsistency in the inversion results of ice sheet model. For each metric, we rank the
194 eight GHF datasets from 1 (least inconsistent) to 8 (most inconsistent). The final score
195 for each dataset is the average of its ranks across the six metrics to ensure a
196 comprehensive evaluation, as a reasonable simulation result should perform well across
197 thawed bed, frozen bed, and the whole region. We only consider grounded ice and
198 exclude points located at the domain boundary due to relatively poor model
199 performance there.

200 The specific metrics that we use to quantify this inconsistency could be adaptable,
201 for example by using a squared error term instead of the linear error terms that we used.
202 However, the general practice of emphasizing and quantifying the inconsistency
203 between a sliding inversion and the temperature/rheology field used as an input to that
204 inversion is novel.

205

206 **2.2 Methodology in Huang et al. (2024)**

207 Huang et al. (2024) employed thermo-mechanical coupled simulations using eight
208 GHF datasets to investigate the steady-state thermal regime of Totten Glacier. The
209 methodology comprised two interconnected modeling components:

- 210 1. Forward Modeling: An enhanced shallow-ice approximation model integrated with
211 a subglacial hydrology module was utilized to simulate englacial temperature profiles.
- 212 2. Inverse Problem: A full-Stokes ice flow model was applied to resolve basal friction
213 coefficients through inverse analysis, to minimize the misfit between simulated and
214 observed velocities while simultaneously generating velocity predictions.

215 A feedback loop was then established: the velocity outputs from the inverse model
216 were used to refine key parameters in the forward model - specifically constraining the
217 basal slip ratio, rheological properties, and shape functions. This bidirectional coupling
218 process underwent multiple iterations to achieve convergent steady-state solutions.

219 Huang et al. (2024) utilized radar specular content data to differentiate localized
220 wet (thawed) versus dry (frozen) basal conditions and used this data as a two-sided
221 constraint on the basal thermal state. They compared modeled basal thermal states
222 derived from different GHFs to evaluate the reliability of the GHF datasets.

223

224 **2.3 Distinction from Huang et al. (2024)**

225 In Huang et al. (2024), modelled surface velocity velocities are compared with
226 observations over the whole domain during the inversion for basal parameters for each
227 GHF dataset. Here, surface velocities act as the observational constraints for the
228 mechanical inversion.

229 Although the overheating metrics here use the surface velocities and can thus be
 230 considered a subset of the inversion residual, our overcooling metrics are based on the
 231 basal sliding velocity derived from the inversion, which is not part of the mechanical
 232 inversion’s residual. A mechanical inversion does not take into account the physical
 233 plausibility of the sliding result it produces. Therefore, it is not circular reasoning to
 234 compare two different parts of a model to each other; rather, it is a check of internal
 235 consistency, or lack thereof. A mechanical inversion may fit the surface velocity
 236 observations equally well when forced with many different models of the ice sheet
 237 thermal structure and rheology; however, if some models require high sliding velocities
 238 in frozen-based regions, then they should be downweighted in comparison to models
 239 that show a good agreement between basal temperature and velocity.

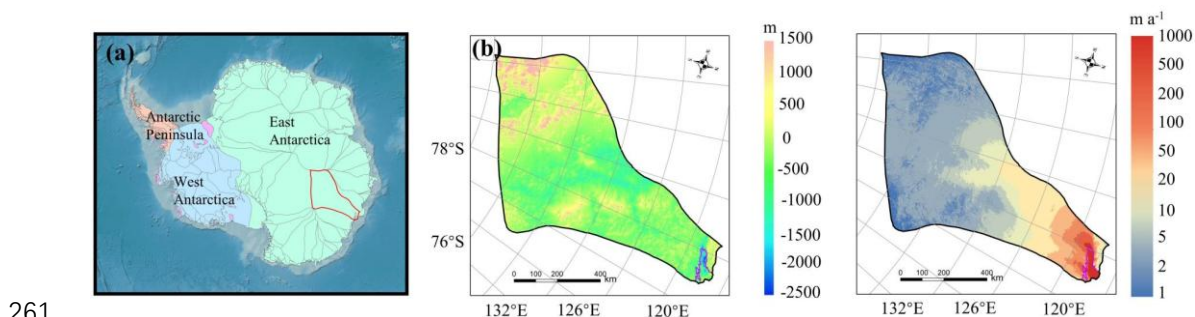
240 The method here does not require any additional observations beyond the surface
 241 velocities used in the mechanical inversion. However, there are “independent
 242 constraints” in the method here, which are not observations, but rather the a priori
 243 physical understandings that: 1) rapid sliding requires warm basal temperatures and
 244 subglacial water; 2) reducing the basal slip coefficient cannot prevent the ice from
 245 flowing by internal shear deformation. The inconsistency metrics developed in this
 246 paper are an attempt to quantify and rank the extent to which these basic (and
 247 uncontroversial) physical understandings are violated.

248

249 3. Application to Totten Glacier with Different GHFs

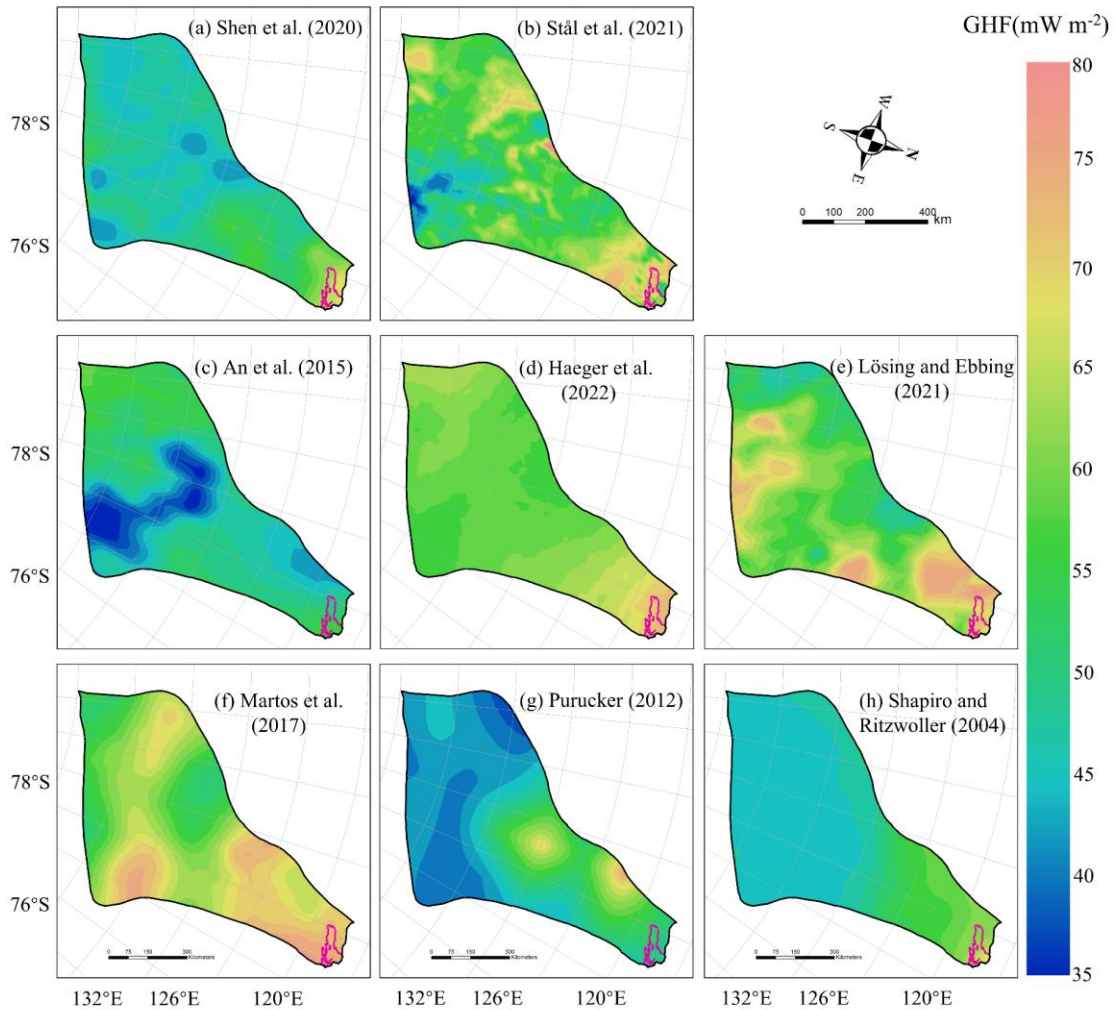
250 3.1 Study domain and Data

251 We apply our method to evaluate simulated ice temperature and ice velocity in
 252 Totten Glacier with eight GHF datasets by Huang et al. (2024) . Huang et al. (2024)
 253 used the present-day surface ice temperature (Le Brocq et al., 2010), observed surface
 254 velocity from MEaSURES InSAR-Based Antarctic Ice Velocity Map, version 2 (Rignot
 255 et al., 2017) and ice sheet topography data from BedMachine Antarctica, version 2
 256 (Morlighem et al., 2020). The eight GHF datasets were derived by various
 257 methodologies, resulting in significant differences in both spatial distribution and
 258 magnitude (Fig. 2). GHF fields from Stål et al. (2021), Haeger et al. (2022), Lösing and
 259 Ebbing (2021) and Martos et al. (2017) generally exhibit higher magnitudes than the
 260 other GHFs.



261

262 **Figure 1. (a)** Geographic location of Totten Glacier (red outline) in Antarctica; **(b)** bed
 263 elevation of Totten Glacier, the purple curve represents the grounding line; **(c)** observed
 264 surface velocity.
 265



266 **Figure 2.** The spatial distribution of the 8 GHF datasets for Totten Glacier **(a–h)** used
 267 as input data in Huang et al. (2024). The purple line depicts the grounding line.
 268
 269

270 The spatial distribution of modelled basal temperature using the 8 GHFs displays
 271 both similarities and heterogeneity. In the northern part of Totten Glacier, there is a
 272 consistent thawed-bedded pattern across all eight simulation results (Fig. S1), which
 273 originates from the grounding line and extends upstream to approximately 71°S. This
 274 thawed-bedded area is not contiguous with the lateral boundaries of Totten Glacier but
 275 is instead bordered by frozen bed. All 8 GHF datasets produce low basal ice
 276 temperatures in the inland southwest, with Purucker et al. (2012), Shapiro and

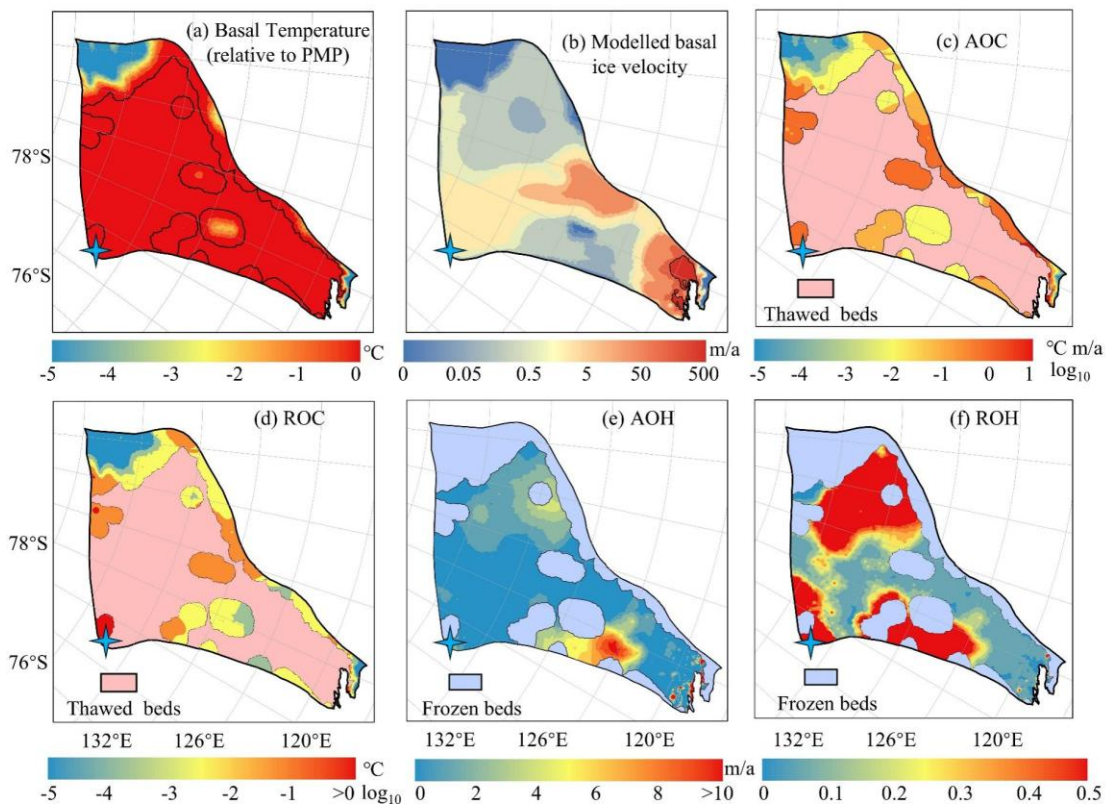
277 Ritzwoller (2004), Shen et al. (2020) and Lösing and Ebbing (2021) being colder. The
 278 basal ice velocities modelled from the 8 different GHF datasets produce similar spatial
 279 distributions (Fig. S2), which can be expected as they were derived using the same
 280 inverse method and constrained by the identical observed surface ice velocity. The
 281 modelled basal ice velocity is fast near the grounding line and its upstream area. There
 282 are also high velocities between 70°S and 72°S close to the western boundary of Totten
 283 Glacier, which are associated with subglacial canyon features in the basal topography
 284 (Fig. 1b) and observed fast surface ice velocity there.

285

286 3.2 Spatial Distribution of Inconsistencies with one GHF dataset

287 In this section, we show the spatial fields of the inconsistency metrics (Section 2.1)
 288 for the modelled result in Huang et al. (2024), using Martos et al. (2017) GHF as an
 289 example. This example illustrates the interpretation process before conducting a
 290 comprehensive comparative analysis for the result with 8 GHF datasets.

291



292

293 Figure 3. Spatial distribution of modelled basal ice temperature (a), modelled basal ice
 294 speed (b), *AOC* (c), *ROC* (d) inconsistencies in modelled frozen-bedded regions, and
 295 *AOH* (e) and *ROH* (f) inconsistencies in modelled thawed-bedded regions associated
 296 with Martos et al. (2017) GHF. The colormap in (c) and (d) is on logarithmic scale. The

297 pink region in (c) and (d) represents modelled thawed bed, while the blue region in (e)
298 and (f) indicates frozen-bedded areas.

299 The modelled result based on the Martos et al. (2017) GHF reveals extensive
300 regions of thawed bed with limited areas of frozen bed. The frozen bed is predominantly
301 located in the southern corner of the study domain, where the modelled basal ice speed
302 approaches zero, consistent with cold basal ice temperature. Consequently, the AOC
303 inconsistency at this marginal zone is negligible (Fig. 3). Along the western margin of
304 Totten Glacier, basal ice temperature remains below the pressure melting point, albeit
305 approaching it. However, localized regions exhibit high basal velocities of several tens
306 of meters per year, contradicting the presence of a frozen bed and resulting in large
307 AOC inconsistencies.

308 Conversely, large AOH values are observed between 69°S and 71°S in the eastern
309 Totten Glacier region, where the simulated surface ice speed exceeds observational data
310 by $>5 \text{ m a}^{-1}$ (Fig. 3e). In this area, the modelled basal ice temperature reaches the
311 pressure melting point, with the modelled basal ice speed at approximately 0.05 m a^{-1} .
312 Basal friction inversion failed to reproduce observed surface ice speed due to the
313 model's overestimation of ice temperature and softness. This pronounced velocity
314 mismatch highlights a fundamental inconsistency in the eastern glacier region, likely
315 originating from discrepancies in the input datasets. Regions of high ROH and ROC
316 values coincide with areas of relatively high AOH and AOC, particularly where the
317 observed surface velocities are slow, as per their formulations.

318

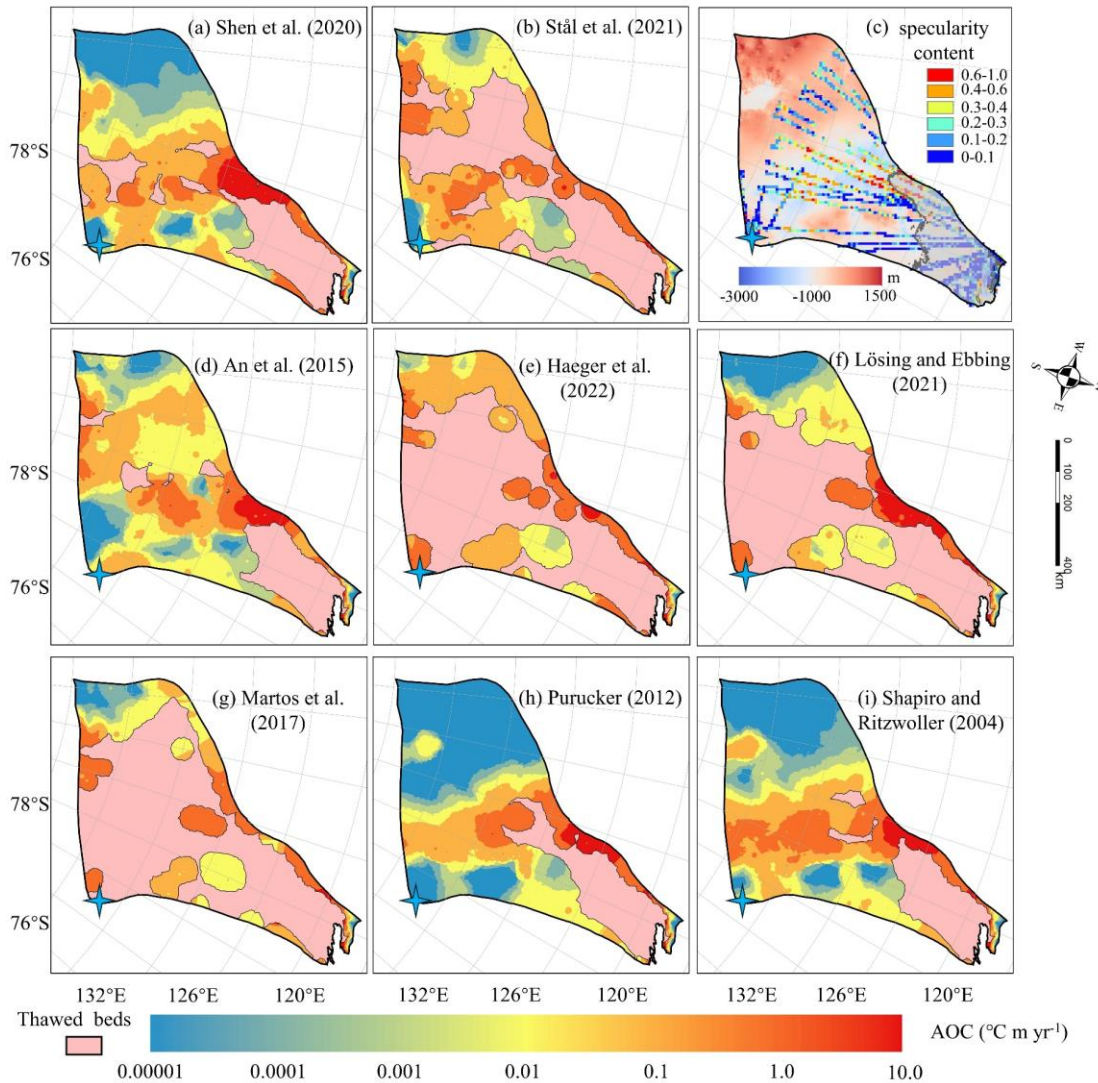
319 **3.3 Spatial Distribution of Inconsistencies** with eight GHF datasets

320 We calculate the absolute inconsistencies, *AOH*, in the thawed bed, and *AOC* in
321 the frozen bed. The spatial distribution of *AOC* reveals that most GHF datasets exhibit
322 significant local overcooling inconsistencies at the subglacial canyon between 70°S and
323 72°S (Fig. 4). There is fast basal sliding in the inverse model results (Fig. S2), however,
324 the modelled basal ice temperatures inferred from most of the GHF datasets are below
325 the pressure melting point (Fig. S1). High specular content in radar data (Fig. 4c)
326 suggests the presence of basal water in the subglacial canyons here (Dow et al., 2020;
327 Huang et al., 2024), which also suggests that the basal ice temperature should be at the
328 pressure melting point and confirms the inconsistency between the modelled
329 temperature and velocity fields.

330 The area near the grounding line is characterized by fast ice flow and thawed bed
331 (Fig. 4), yet some of the margin is frozen-bedded with modelled basal temperature
332 below the pressure melting point, resulting in high *AOC*. Overall, modelled results with
333 most GHF datasets show small overcooling inconsistencies. The modelled results using
334 GHF from Purucker et al. (2012), Shapiro and Ritzwoller (2004), Shen et al. (2020),
335 Lösing and Ebbing (2021) exhibit no overcooling inconsistency in southwestern Totten

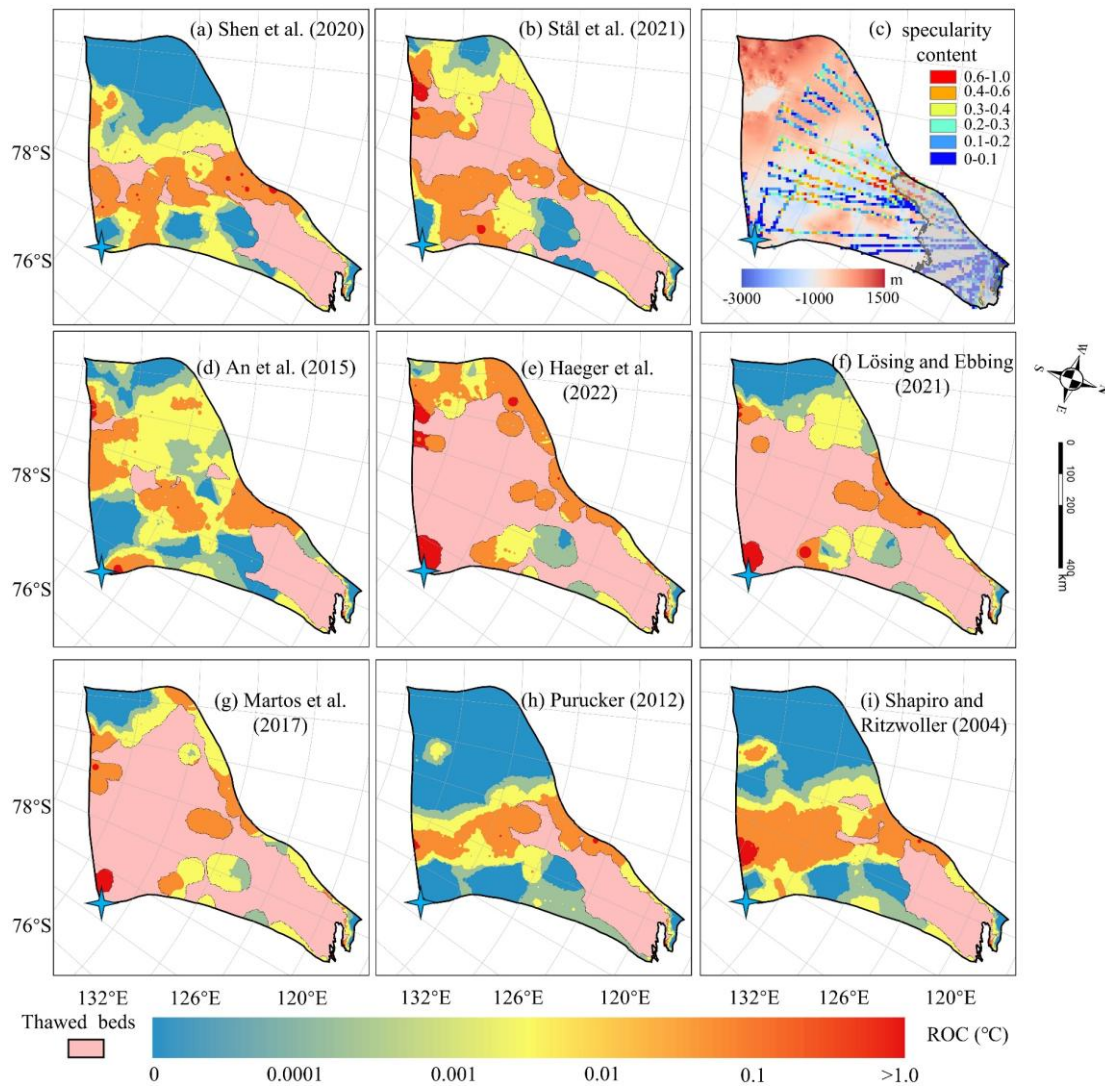
336 Glacier (Fig. 4).

337 The spatial distribution of relative overcooling inconsistencies, *ROC* (Fig. 5),
338 differs from that of absolute inconsistencies, *AOC*, and is due to the spatial variability
339 in surface ice speed. The largest value of *ROC* across most GHF occurs at Dome C,
340 where the observed surface ice speed is close to zero.
341



342

343 **Figure 4.** Spatial distribution of *AOC* inconsistency in modelled frozen-bedded regions
344 **(a-b, d-i)** associated with the GHFs **(a-h)** in Fig. 2. The colormap is on logarithmic
345 scale. The pink region represents modelled thawed bed. **(c)** Specularity content sourced
346 from radar data collected by ICECAP (Dow et al., 2020) with the bed elevation in the
347 background. Gray area in **(c)** corresponds to surface speed exceeding 30 m yr⁻¹. The
348 blue star represents Dome C.

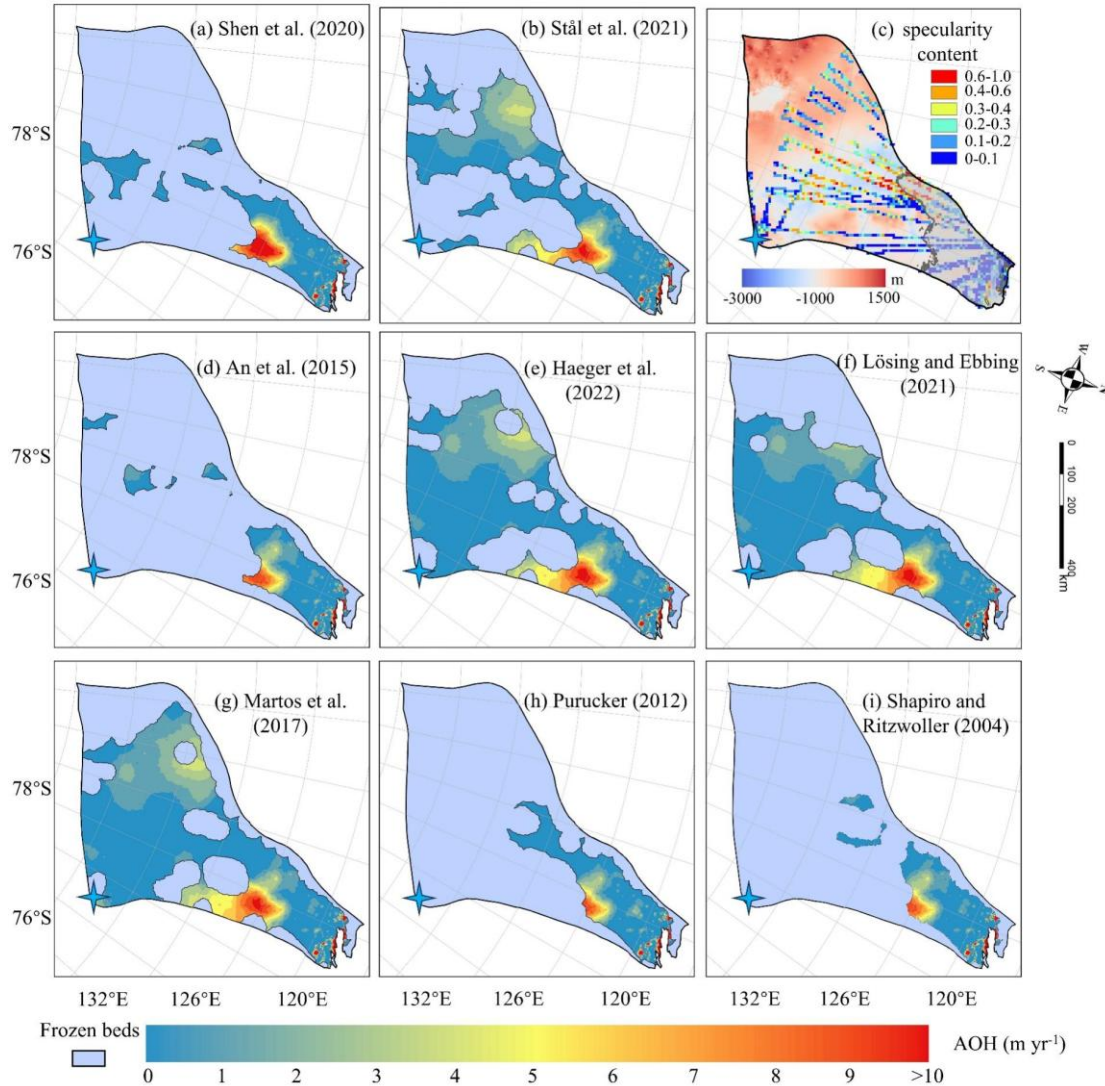


350
 351 Figure 5. The spatial distribution of relative overcooling (ROC) inconsistency in cool
 352 beds with (a), (b) and (d) to (i) corresponding to the GHFs (a - h) in Figure 2. The pink
 353 area represents the thawed beds. Dome C is marked by a blue star. (c) Locations of
 354 specularity content derived from radar data collected by ICECAP (Dow et al., 2020)
 355 and with the bed elevation in the background. The gray curve is the contour of the
 356 surface speed of 30 m yr^{-1} . Note the colormap is non-linear.

357

358 The GHF datasets of Stål et al. (2021), Haeger et al. (2022), Lösing and Ebbing
 359 (2021) and Martos et al. (2017) which have higher than average GHF values provide
 360 larger areas of thawed bed than the other 4 GHFs. The simulations with all 8 GHFs
 361 yield similar spatial distributions of *AOH* (Fig. 6) on the common area of thawed bed,
 362 and similar locations of high *AOH* values. A common high *AOH* area is located between

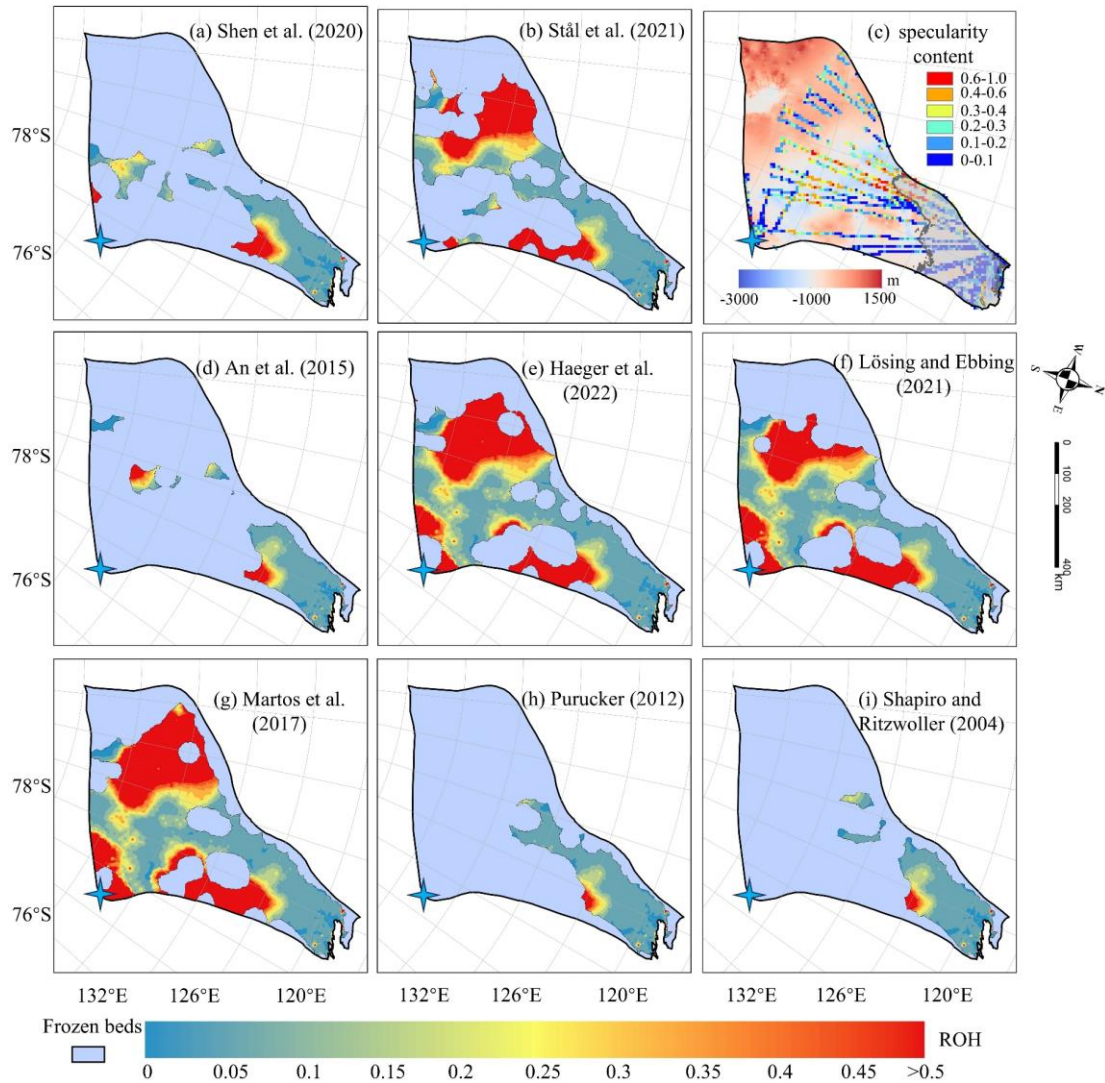
363 69°S and 72°S in the eastern part of Totten Glacier, due to simulated surface ice
 364 velocities greatly exceeding the observed surface ice velocities. Low specularity
 365 content from radar data (Fig. 6c) suggests there is no basal water in the area (Dow et
 366 al., 2020; Huang et al., 2024). Therefore, it is likely that the basal ice temperature is
 367 overestimated there. The simulations with all the 8 GHFs also yield similar spatial
 368 distribution of *ROH* (Fig. 7), but its largest values are mostly in the slow flowing region
 369 as one may expect from its formulation (Eq. (3)).



370

371 **Figure 6.** Spatial distribution of *AOH* in thawed-bedded regions with (a-b, d-i)
 372 corresponding to the GHFs (a-h) in Fig. 2. The blue region indicates frozen-bedded
 373 areas. (c) Locations of specularity content, same as Fig. 4c. The blue star represents
 374 Dome C.

375



376

377 Figure 7. The spatial distribution of relative overheating (ROH) inconsistency in
 378 thawed beds with (a), (b) and (d) to (i) corresponding to the GHFs (a - h) in Figure 2.

379 The light purple mask represents the frozen beds. (c) Locations of specularity content
 380 (coloured points), same as Fig. 6.

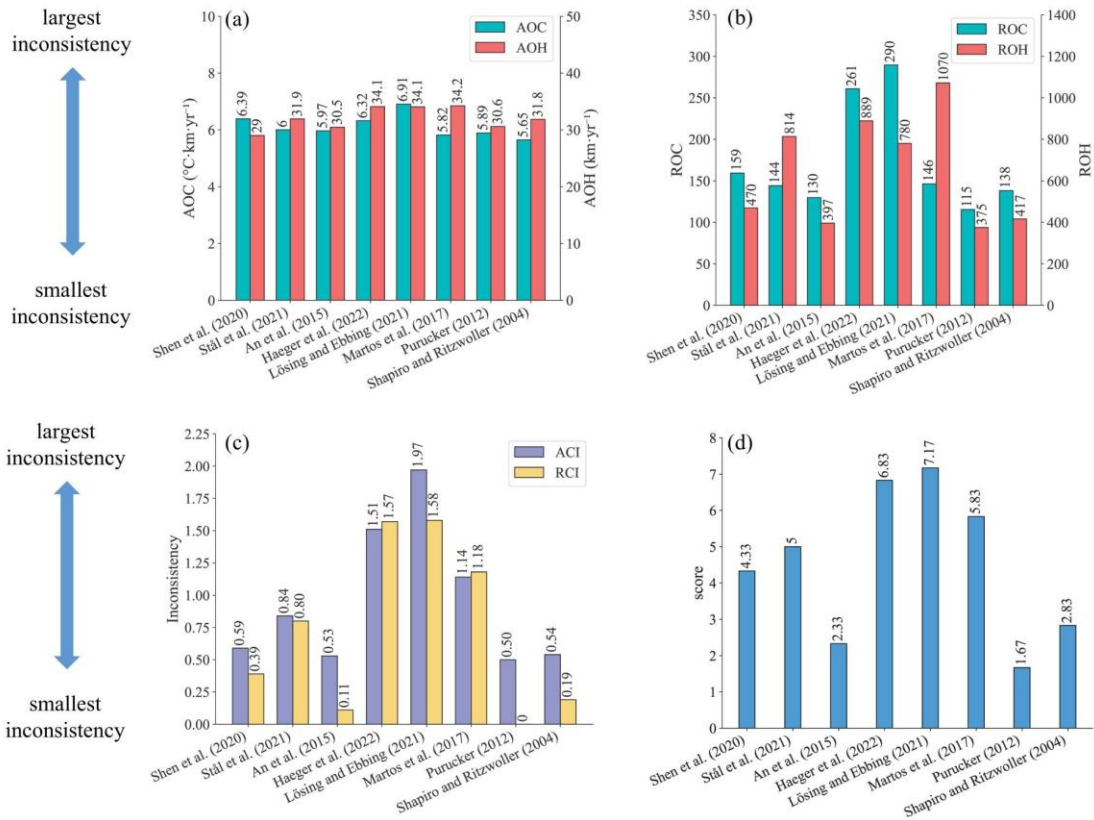
381

382 3.4 Evaluation of Model Inconsistency with Eight GHFs

383 To assess the overall inconsistency of each geothermal heat flux dataset, we
 384 calculate the sum of each metric over all points. All inconsistency indices for the
 385 simulation results using the eight GHF datasets are illustrated in Fig. 8. The overheating
 386 inconsistency associated with Purucker et al. (2012) and Shapiro and Ritzwoller (2004)
 387 GHFs is predominantly localized in fast-flowing regions. Consequently, after
 388 normalization by the surface observed ice speed, their relative rankings improve (Fig.
 389 8). The GHFs from Purucker et al. (2012), An et al. (2015), Shapiro and Ritzwoller

390 (2004), and Shen et al. (2020) demonstrate balanced performance with respect to both
391 overheating and overcooling inconsistency metrics, thereby securing the top four
392 positions in both *ACI* and *RCI*. Their *ACI* values exhibit similarity, ranging from 0.50
393 to 0.59 (Fig. 8c). In contrast, simulation result utilizing Martos et al. (2017) GHF
394 exhibits low *AOC* but high *AOH*. Simulation results utilizing Stål et al. (2021) GHF
395 show low *ROC* but relatively high *ROH*. Notably, simulation results employing GHFs
396 from Martos et al. (2017), Haeger et al. (2022), and Lösing and Ebbing (2021)
397 demonstrate comparably high *AOH* values. These four GHF datasets—Martos et al.
398 (2017), Stål et al. (2021), Haeger et al. (2022), and Lösing and Ebbing (2021)—are
399 ranked in the bottom four positions for both *ACI* and *RCI* metrics. Furthermore, the
400 ranking order of the eight GHFs remains consistent between *ACI* and *RCI*.

401 The final averaged ranking (Fig. 8d) across the indices is also the same as that of
402 *ACI* and *RCI*. Purucker et al. (2012), An et al. (2015) and Shapiro and Ritzwoller (2004)
403 GHFs occupy the top three positions. Following closely, Shen et al. (2020) and Stål et
404 al. (2021) GHFs secure the 4th and 5th positions, respectively. Martos et al. (2017),
405 Haeger et al. (2022) and Lösing and Ebbing (2021) GHFs are ranked as the bottom
406 three among the eight GHFs in Totten Glacier. The thermal state produced by the
407 optimal GHF result shows that thawed beds predominantly cluster around the
408 grounding line and its upstream regions. Conversely, the inland areas of Totten largely
409 exhibit cold temperatures, with relatively sparse thawed-bedded areas.



410
 411 **Figure 8.** Six inconsistency indicators and the final ranking of 8 GHF datasets. **(a)** the
 412 absolute overcooling and overheating inconsistencies, *AOC* and *AOH*; **(b)** the relative
 413 overcooling and overheating inconsistencies, *ROC* and *ROH*; **(c)** the absolute and
 414 relative combined inconsistencies, *ACI* and *RCI*; **(d)** the average of ranking scores from
 415 1 to 8 using the six inconsistency indicators. The value of inconsistencies and scores
 416 are labeled at the top of the bars.

417

418 4. Discussion

419 4.1 Causes of Inconsistencies and Sources of Uncertainty

420 Our method evaluates the quality of an ice sheet temperature field by quantifying
 421 the inconsistency between that temperature field and the velocity field that is obtained
 422 if that temperature field is used to compute the rheology in a mechanical inversion.
 423 Because mechanical inversions use surface velocity observations as a constraint, we
 424 have developed an indirect method for using surface velocity observations to check the
 425 quality of an englacial temperature simulation. However, the mere fact that
 426 inconsistencies exist does not by itself tell us what caused those inconsistencies.

427 Broadly speaking, the measured inconsistencies can come from two sources:
 428 temperature or velocity. Uncertainties in any of the input datasets used to compute those
 429 two fields can produce inconsistencies, as can simplifications in the model physics.

430 Here, we have tested the influence of one particular boundary condition, GHF, since
431 that field is particularly hard to constrain. Because all other inputs are kept constant,
432 the differences in the inconsistencies that we calculated between different simulations
433 can be attributed to the GHF fields. However, we also found that all of the models we
434 tested had non-zero inconsistency (Fig. 4; Fig. 6). The absolute inconsistencies, *AOH*
435 and *AOC*, had particularly small between-model variability in comparison to their mean
436 value. This could be because none of the input GHF fields correctly captured the true
437 GHF, but it could also indicate problems with other model inputs. For instance, the
438 surface temperature used in Huang et al. (2024) represents the present-day climate, but
439 the thermal structure of the ice sheet may reflect colder temperatures during the last
440 glacial cycle. We discuss an additional experiment we performed to test the influence
441 of uncertainty in surface temperature on our inconsistency metrics in Section 4.3 below.
442 By contrast, surface accumulation rate should have been lower during glacial periods,
443 which would have a warming influence on ice sheet temperatures. Uncertainties in bed
444 topography should influence both our thermal and our mechanical models, with deeper
445 ice being more likely to be warm, and with errors in ice thickness producing
446 compensating errors in basal sliding in our mechanical inversion. In the study of Huang
447 et al. (2024), BedMachine v2 was used for ice thickness and subglacial topography.
448 However, Bedmap3 (Pritchard et al., 2025) has better-resolved mountains and smoother
449 trough margins.

450 The simulation results we use from Huang et al. (2024) came from a 3D isotropic
451 full-Stokes ice flow model. While full-Stokes is generally considered the gold standard
452 of ice sheet mechanical modeling, the use of an isotropic rheology may not be valid in
453 some parts of the ice sheet, such as near ice divides or at the margin of an ice stream
454 where the history of past ice deformation creates anisotropic crystal fabric that affects
455 the present-day mechanical properties (Martín et al., 2009; Zhao et al., 2018b; Zwinger
456 et al., 2014). Isotropic flow laws often require the use of an “enhancement factor” for
457 vertical shear in the lower part of the ice column, an ad hoc correction that would have
458 a particularly large influence on our computed overcooling metrics. Thus the isotropic
459 flow law potentially introduces errors in modelled strain rates and, hence, bias in basal
460 sliding velocities obtained by inversion methods (Budd and Jacka, 1989; Gerber et al.,
461 2023; Rathmann and Lilien, 2022). Simulated surface ice velocities can be influenced
462 by other factors in addition to ice fabric; shear margins are also impacted by
463 accumulated rupture, such as damage along a shear margin (e.g., Benn et al., 2022;
464 Lhermitte et al., 2020; Schoof, 2004; Sun et al., 2017). Ice deposited during the last
465 glaciation has different chemistry (especially concentrations of chloride and possibly
466 sulphate ions) which leads to smaller crystals that develop a strong, near-vertical,
467 single-maximum fabric (Paterson, 1991). However, ice fabric data is sparse, known
468 from direct observations at ice cores (Azuma and Higashi, 1985) or inferred from

469 specialized radar measurements (Fujita and Mae, 1994; Jordan et al., 2022), and its
470 impact beyond the scope of this study as we refrain from incorporating additional
471 observational data relying only on widely-available surface ice velocities.

472 Our inconsistency metrics are designed to provide bidirectional constraints,
473 wherein the model is penalized for both overheating and overcooling. By adopting this
474 bidirectional constraint framework, we aim to mitigate the risk of unidirectional
475 constraints leading to excessively cold or warm outcomes being deemed optimal.
476 However, our inconsistency metrics only provide a bidirectional constraint when
477 viewed in a spatially integrated sense. Locally, we only have unidirectional constraints.
478 This is because our overheating metrics are only computed where the bed is at the
479 melting point, and our overcooling metrics are only computed where the bed is below
480 the melting point. This makes methodological sense, as we know for sure that sliding
481 must only occur where the bed is thawed. However, in reality it is entirely possible that
482 some of the areas where the modelled bed reaches the pressure melting point are still
483 too cold (the modelled melt rate is lower than the real melt rate), and conversely, it is
484 also possible that some of the areas where the modelled bed is below the pressure
485 melting point are still too warm (the real temperature is colder still). Our method cannot
486 identify these areas. Thus, our inconsistency metrics may underestimate variability in
487 the ice sheet thermal state: we have no way to penalize frozen regions that are not cold
488 enough or thawed regions that are not warm enough. We leave the development of these
489 constraints to future work.

490

491 **4.2 Sensitivity of Inconsistencies to GHF Datasets**

492 Comparing the GHF dataset rankings between this study and Huang et al. (2024),
493 we find that the top 4 and the bottom 4 are the same in the two studies, albeit with slight
494 variations in ranking. The lower ranking of Shen et al. (2020) in this study may be
495 attributed to several factors. Firstly, Huang et al. (2024) excludes areas with ice speed
496 exceeding 30 m a^{-1} (Fig. 4c) because specular content is an ambiguous indicator of
497 wet beds there. Secondly, the GHF from Shen et al. (2020) yields higher basal
498 temperature and also faster basal ice velocities in most of the frozen bed of Totten
499 Glacier, hence exhibits greater overcooling inconsistency, compared with Purucker et
500 al. (2012), leading to a decrease in its rankings (Fig. S3). Lastly, Huang et al. (2024)
501 primarily relied on specular content, while our study evaluated datasets based on
502 inconsistencies in the simulation results. Despite these methodological differences, both
503 studies identified four relatively well-performing GHF datasets for Totten Glacier,
504 which exhibit similar distributions of thawed and frozen beds when compared to the
505 other four datasets (Fig. 4 and Fig. 6). This similarity underscores that the thawed bed
506 is concentrated near and upstream of the grounding line. Datasets from Stål et al. (2021),

507 Martos et al. (2017), Haeger et al. (2022), and Lösing and Ebbing (2021) exhibit a
508 tendency to overestimate GHF in central Totten Glacier.

509 Simulations employing GHF datasets from Stål et al. (2021), Martos et al. (2017),
510 Haeger et al. (2022), and Lösing and Ebbing (2021) yield more extensive thawed-
511 bedded regions and are expected to exhibit greater overheating inconsistency.
512 Nevertheless, these models also exhibit relatively high overcooling inconsistency
513 despite the limited extent of frozen-bedded regions. We quantified the discrepancies
514 between these four GHF datasets and the Purucker et al. (2012) GHF in terms of
515 modelled basal velocity, basal temperature relative to the pressure melting point, and
516 *AOC* (Fig. S5). The Purucker et al. (2012) GHF yields lower basal ice temperatures and
517 slower basal velocities across most frozen-bedded regions, consequently resulting in
518 lower *AOC* values compared to the other four GHF datasets.

519

520 **4.3 Implications for Ice Sheet Dynamics**

521 While evaluating inconsistencies highlights the spatial distribution of mismatches,
522 it does not inherently elucidate their underlying causes. The primary factors to
523 investigate are surface temperature, GHF, accumulation rate, and ice thickness,
524 representing the most critical boundary conditions. Furthermore, integrating multiple
525 sources of prior knowledge can help constrain model parameters:

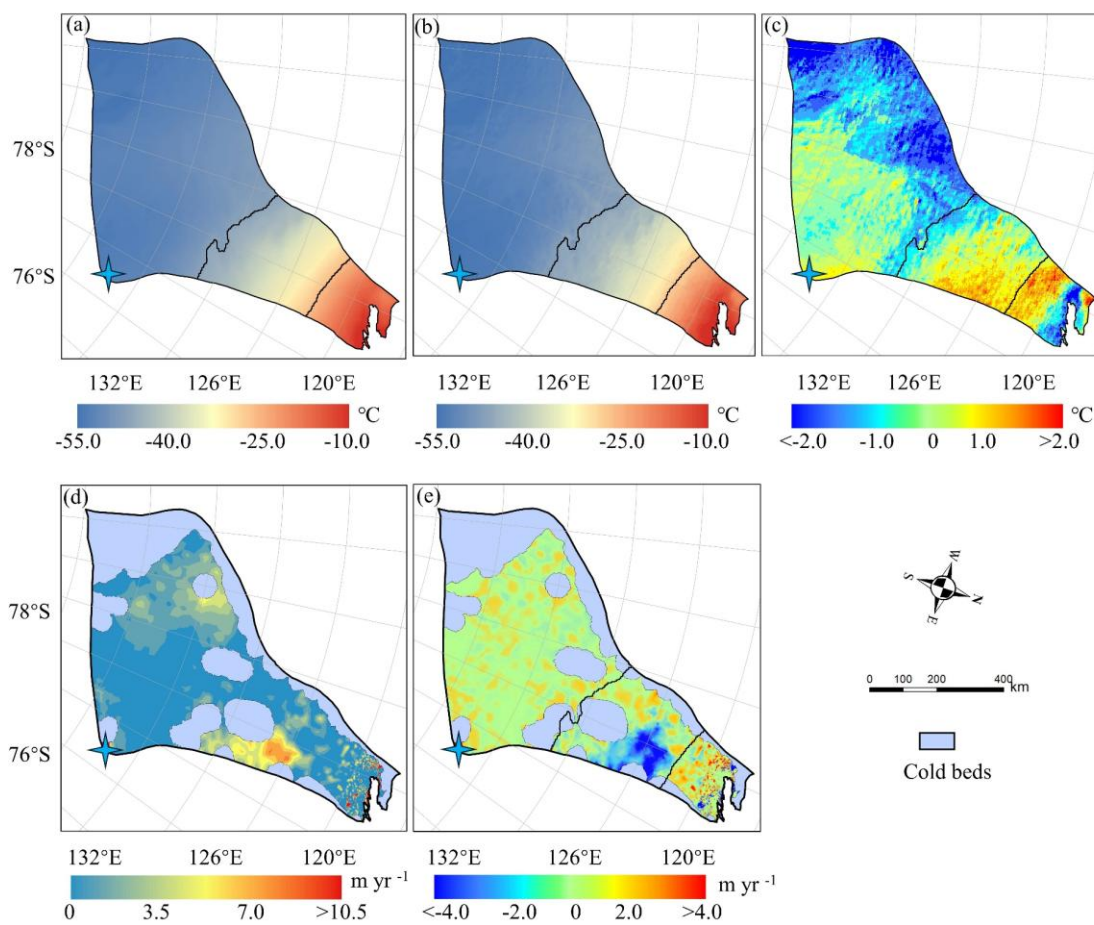
526 1. High-resolution radar measurements: The availability of ice thickness data along
527 flight lines should be assessed to validate geometric boundary conditions.

528 2. Paleoclimate context: Historical climate reconstructions indicate significantly colder
529 surface temperatures during glacial periods compared to present-day conditions, with
530 correspondingly lower accumulation rates. These paleo-temperature conditions likely
531 induced a long-term thermal memory within the ice column, potentially contributing to
532 observed discrepancies between modeled and measured basal properties.

533 Therefore, we recommend a systematic evaluation of: (1) The spatial distribution
534 of radar-derived ice thickness measurements; (2) The temporal consistency of surface
535 temperature boundary conditions; (3) The sensitivity of model results to GHF variations;
536 (4) Accumulation rate reconstructions during key climatic periods. This multi-faceted
537 approach helps isolate the causes of inconsistencies in ice sheet simulations.

538 There is a common area between 69°S and 72°S in the eastern part of Totten
539 Glacier with the largest *AOH* (Fig. 6) for all the GHFs varying from 48 to 70 mW m⁻²,
540 which suggests that the *AOH* inconsistency is from other ice sheet properties rather than
541 GHF. Zhang et al. (2022) reconstructed Antarctic near-surface air temperature based on
542 MODIS land surface temperature measurements and in situ air temperature records
543 from meteorological stations from 2001 to 2018. We compared the reconstruction of
544 near-surface air temperature in the year 2001 (Zhang et al., 2022) and the ALBMAP v1
545 dataset used in Huang et al. (2024). The surface air temperature in the area with large

546 *AOH* from ALBMAP v1 is 0.6-3.1 °C higher than that from the reconstructed near-
 547 surface air temperature in 2001 (Fig. 9). The MODIS-based near-surface air
 548 temperature product shows warming in Totten Glacier from 2001 to 2018. Even so, the
 549 surface air temperature in the area with large *AOH* from ALBMAP v1 is still higher
 550 than that in 2018 but over a smaller area. Therefore, we infer that the large *AOH* may
 551 be attributed to the present-day ice surface temperature derived from ALBMAP v1 in
 552 this area being unrealistically warm. The englacial temperature will be lower than
 553 present-day ice sheet surface temperature used in the model but warmer than the
 554 average surface temperature during the last glacial-interglacial cycle. We lowered the
 555 surface ice temperature in this area by 1 °C, reran the simulation, and found that *AOH*
 556 with all the GHFs was halved (Fig. 9e).
 557



558
 559 **Figure 9.** Surface ice temperature from ALBMAP v1 (a) and MODIS-based near-
 560 surface air temperature (b) in the year 2001, and their difference (c). (d) The *AOH* using
 561 modified surface ice temperature by reducing the temperature between the two thick
 562 black curves (contour lines of -44 °C and -26 °C) in (a) by 1 °C and GHF of Martos

563 et al. (2017). (e) The difference between the AOH using cooler surface ice temperature
564 and the original AOH. The blue star represents Dome C.

565 Given that data assimilation and inverse methods are widely employed to infer
566 basal friction coefficients in ice sheet simulations, it is essential to acknowledge the
567 impact of the inconsistencies identified in our study on ice sheet dynamics. A frozen
568 bed is supposed to provide substantial resistance and limit basal sliding; however, if the
569 basal temperature is overestimated, it may decrease viscosity and enhance basal sliding.
570 This overheating inconsistency would lead to an overestimation of ice flow speeds,
571 discharge, and the dynamic ice loss (Artemieva, 2022; Burton-Johnson et al., 2020).
572 Similarly, under representation of thawed bedding would slow ice discharge estimates,
573 and hence potential ice sheet response to climate warming. The basal thermal regime
574 critically influences the stability of grounding lines and the behavior of ice streams. In
575 a warming climate, increases in geothermal or frictional heating can trigger basal
576 thawing in these areas, lowering basal friction and potentially initiating rapid grounding
577 line retreat—a key component of marine ice sheet instability (MISI) (Reese et al., 2023;
578 Ross et al., 2012). Without incorporating a self-consistent thermal model into the
579 inversion, projections may misrepresent the onset and extent of these dynamic
580 instabilities. Our findings underscore that a fully coupled inversion framework would
581 use not only surface velocity data but also incorporate direct or proxy observations of
582 basal temperature and subglacial hydrology. Such an approach would better constrain
583 the basal friction coefficient in a physically consistent manner, reducing the risk of
584 producing nonphysical states. This integration is especially critical for projections of
585 ice sheet evolution under climate change, as the dynamic response is sensitive to even
586 small changes in basal conditions.

587

588 **5. Conclusion**

589 We propose a novel and rapid method to quantify the inconsistencies between
590 modelled basal ice temperature and observed surface ice speed and assess the quality
591 of ice sheet model simulation results without using subglacial observation data.
592 Previously, it has been assumed that checking the quality of an ice sheet temperature
593 model required in situ observations, whether from ice cores or geophysical techniques
594 like ice penetrating radar. By using the ice temperature field to compute the rheology
595 structure needed for a mechanical inversion and then quantifying the inconsistency
596 between the inverted velocity field and the original ice temperature field, we are able
597 to use remotely sensed surface velocity observations as a check on the quality of
598 modelled englacial temperatures. Given the challenges in acquiring subglacial data, our
599 method can provide a streamlined and effective approach to evaluation.

600 We apply this method to the simulation results of Totten Glacier using a 3D full-
601 Stokes model with 8 different GHF datasets. Assuming the inconsistencies are mainly

602 due to unrealistic GHF datasets, we use the inconsistencies to assess the reliability of
603 those GHF datasets. We compare our GHF ranking with that by Huang et al. (2024)
604 which used specularity content to derive a two-sided constraint on the basal thermal
605 state. We find that the top 4 and the bottom 4 GHFs are the same in the two studies,
606 albeit with slight variations in ranking. Furthermore, we find that the simulations with
607 all GHF datasets underestimate the basal ice temperature in a canyon on the western
608 boundary of Totten Glacier, and we infer that the common high overheating
609 inconsistencies with all the GHF datasets in the eastern Totten Glacier between 69°S
610 and 72°S may be attributed to the unrealistically warm surface ice temperature used
611 there in the model. While we demonstrate that this approach works on simulation results
612 for Totten Glacier, testing of the method on other glaciers would be useful to assess if
613 the approach is worthwhile for revealing ambiguous conflicts in observations and
614 simulations.

615

616

617

618 *Data availability.* MEaSURES BedMachine Antarctica, version 2, is available at
619 <https://doi.org/10.5067/E1QL9HFQ7A8M> (Morlighem, 2020). MEaSURES InSAR-
620 Based Antarctic Ice Velocity Map, version 2, is available at
621 <https://doi.org/10.5067/D7GK8F5J8M8R> (Rignot et al., 2017). MEaSURES Antarctic
622 Boundaries for IPY 2007–2009 from Satellite Radar, version 2, is available at
623 <https://doi.org/10.5067/AXE4121732AD> (Mouginot et al., 2017). ALBMAP v1 and the
624 GHF dataset of Shapiro and Ritzwoller (2004) are available at
625 <https://doi.org/10.1594/PANGAEA.734145> (Le Brocq et al., 2010b). The GHF dataset
626 of An et al. (2015) is available at
627 <http://www.seismolab.org/model/antarctica/lithosphere/AN1-HF.tar.gz> (last access: 11
628 April 2023). The GHF dataset of Shen et al. (2020) is available at
629 <https://sites.google.com/view/weisen/research-products?authuser=0> (last access: 11
630 April 2023). The GHF dataset of Martos (2017) is available at
631 <https://doi.org/10.1594/PANGAEA.882503>. The GHF dataset of Purucker (2012) is
632 available at
633 https://core2.gsfc.nasa.gov/research/purucker/heatflux_mf7_foxmaule05.txt (last
634 access: 11 April 2023).

635

636 *Author contributions.* LZ and JCM conceived the study. LZ, MW, and JCM designed
637 the methodology. JW and LZ analyzed the data and conducted visualization. JW
638 and LZ wrote the original draft, and all the authors revised the paper.

639

640 *Competing interests.* The contact author has declared that none of the authors has any

641 competing interests.

642

643 *Acknowledgements.* This work was supported by National Natural Science Foundation
644 of China (grant no. 42576280) and Academy of Finland (grant no. 355572).

645

646 **References**

- 647 Albrecht, T., Winkelmann, R., and Levermann, A.: Glacial-cycle simulations of the Antarctic Ice
648 Sheet with the Parallel Ice Sheet Model (PISM) – Part 1: Boundary conditions and climatic
649 forcing, *The Cryosphere*, 14, 599–632, <https://doi.org/10.5194/tc-14-599-2020>, 2020.
- 650 An, M., Wiens, D. A., Zhao, Y., Feng, M., Nyblade, A., Kanao, M., Li, Y., Maggi, A., and L  v  que,
651 J.: Temperature, lithosphere-asthenosphere boundary, and heat flux beneath the Antarctic Plate
652 inferred from seismic velocities, *J. Geophys. Res. Solid Earth*, 120, 8720–8742,
653 <https://doi.org/10.1002/2015JB011917>, 2015.
- 654 Artemieva, I. M.: Antarctica ice sheet basal melting enhanced by high mantle heat, *Earth-Sci. Rev.*,
655 226, 103954, <https://doi.org/10.1016/j.earscirev.2022.103954>, 2022.
- 656 Azuma, N. and Higashi, A.: Formation Processes of Ice Fabric Pattern in Ice Sheets, *Ann. Glaciol.*,
657 6, 130–134, <https://doi.org/10.3189/1985AoG6-1-130-134>, 1985.
- 658 Benn, D. I., Luckman, A.,   str  m, J. A., Crawford, A. J., Cornford, S. L., Bevan, S. L., Zwinger, T.,
659 Gladstone, R., Alley, K., Pettit, E., and Bassis, J.: Rapid fragmentation of Thwaites Eastern Ice
660 Shelf, *The Cryosphere*, 16, 2545–2564, <https://doi.org/10.5194/tc-16-2545-2022>, 2022.
- 661 Brondex, J., Gagliardini, O., Gillet-Chaulet, F., and Durand, G.: Sensitivity of grounding line
662 dynamics to the choice of the friction law, *J. Glaciol.*, 63, 854–866,
663 <https://doi.org/10.1017/jog.2017.51>, 2017.
- 664 Brondex, J., Gillet-Chaulet, F., and Gagliardini, O.: Sensitivity of centennial mass loss projections
665 of the Amundsen basin to the friction law, *The Cryosphere*, 13, 177–195,
666 <https://doi.org/10.5194/tc-13-177-2019>, 2019.
- 667 Budd, W. F. and Jacka, T. H.: A review of ice rheology for ice sheet modelling, *Cold Reg. Sci.*
668 *Technol.*, 16, 107–144, [https://doi.org/10.1016/0165-232X\(89\)90014-1](https://doi.org/10.1016/0165-232X(89)90014-1), 1989.
- 669 Budd, W. F., Keage, P. L., and Blundy, N. A.: Empirical Studies of Ice Sliding, *J. Glaciol.*, 23, 157–
670 170, <https://doi.org/10.3189/S0022143000029804>, 1979.
- 671 Burton-Johnson, A., Dziadek, R., and Martin, C.: Review article: Geothermal heat flow in
672 Antarctica: current and future directions, *The Cryosphere*, 14, 3843–3873,
673 <https://doi.org/10.5194/tc-14-3843-2020>, 2020.
- 674 Choi, Y., Seroussi, H., Morlighem, M., Schlegel, N.-J., and Gardner, A.: Impact of time-dependent
675 data assimilation on ice flow model initialization and projections: a case study of Kjer Glacier,
676 Greenland, *The Cryosphere*, 17, 5499–5517, <https://doi.org/10.5194/tc-17-5499-2023>, 2023.
- 677 Cornford, S. L., Martin, D. F., Payne, A. J., Ng, E. G., Le Brocq, A. M., Gladstone, R. M., Edwards,
678 T. L., Shannon, S. R., Agosta, C., Van Den Broeke, M. R., Hellmer, H. H., Krinner, G.,
679 Ligtenberg, S. R. M., Timmermann, R., and Vaughan, D. G.: Century-scale simulations of the
680 response of the West Antarctic Ice Sheet to a warming climate, *The Cryosphere*, 9, 1579–1600,

681 <https://doi.org/10.5194/tc-9-1579-2015>, 2015.

682 Dow, C. F., McCormack, F. S., Young, D. A., Greenbaum, J. S., Roberts, J. L., and Blankenship, D.
683 D.: Totten Glacier subglacial hydrology determined from geophysics and modeling, *Earth*
684 *Planet. Sci. Lett.*, 531, 115961, <https://doi.org/10.1016/j.epsl.2019.115961>, 2020.

685 Dziadek, R., Gohl, K., Diehl, A., and Kaul, N.: Geothermal heat flux in the Amundsen Sea sector
686 of West Antarctica: New insights from temperature measurements, depth to the bottom of the
687 magnetic source estimation, and thermal modeling, *Geochem. Geophys. Geosystems*, 18,
688 2657–2672, <https://doi.org/10.1002/2016GC006755>, 2017.

689 Fisher, A. T., Mankoff, K. D., Tulaczyk, S. M., Tyler, S. W., and Foley, N.: High geothermal heat
690 flux measured below the West Antarctic Ice Sheet, *Sci. Adv.*, 1(6), e1500093,
691 <https://doi.org/10.1126/sciadv.1500093>, 2015.

692 Fowler, A. C.: A theoretical treatment of the sliding of glaciers in the absense of cavitation, *Philos.*
693 *Trans. R. Soc. Lond. Ser. Math. Phys. Sci.*, 298, 637–681,
694 <https://doi.org/10.1098/rsta.1981.0003>, 1981.

695 Fujita, S. and Mae, S.: Strain in the ice sheet deduced from the crystal-orientation fabrics from bare
696 icefields adjacent to the Sør-Rondane Mountains, Dronning Maud Land, East Antarctica, *J.*
697 *Glaciol.*, 40, 135–139, <https://doi.org/10.3189/S0022143000003907>, 1994.

698 Gagliardini, O., Cohen, D., Råback, P., and Zwinger, T.: Finite-element modeling of subglacial
699 cavities and related friction law, *J. Geophys. Res. Earth Surf.*, 112, F02027,
700 <https://doi.org/10.1029/2006JF000576>, 2007.

701 Gerber, T. A., Lilien, D. A., Rathmann, N. M., Franke, S., Young, T. J., Valero-Delgado, F., Ershadi,
702 M. R., Drews, R., Zeising, O., Humbert, A., Stoll, N., Weikusat, I., Grinsted, A., Hvidberg, C.
703 S., Jansen, D., Miller, H., Helm, V., Steinhage, D., O’Neill, C., Paden, J., Gogineni, S. P., Dahl-
704 Jensen, D., and Eisen, O.: Crystal orientation fabric anisotropy causes directional hardening of
705 the Northeast Greenland Ice Stream, *Nat. Commun.*, 14, 2653, [https://doi.org/10.1038/s41467-](https://doi.org/10.1038/s41467-023-38139-8)
706 023-38139-8, 2023.

707 Gillet-Chaulet, F., Gagliardini, O., Seddik, H., Nodet, M., Durand, G., Ritz, C., Zwinger, T., Greve,
708 R., and Vaughan, D. G.: Greenland ice sheet contribution to sea-level rise from a new-
709 generation ice-sheet model, *The Cryosphere*, 6, 1561–1576, [https://doi.org/10.5194/tc-6-1561-](https://doi.org/10.5194/tc-6-1561-2012)
710 2012, 2012.

711 Gladstone, R., Schäfer, M., Zwinger, T., Gong, Y., Strozzi, T., Mottram, R., Boberg, F., and Moore,
712 J. C.: Importance of basal processes in simulations of a surging Svalbard outlet glacier, *The*
713 *Cryosphere*, 8, 1393–1405, <https://doi.org/10.5194/tc-8-1393-2014>, 2014.

714 Greenbaum, J. S., Blankenship, D. D., Young, D. A., Richter, T. G., Roberts, J. L., Aitken, A. R. A.,
715 Legresy, B., Schroeder, D. M., Warner, R. C., van Ommen, T. D., and Siegert, M. J.: Ocean
716 access to a cavity beneath Totten Glacier in East Antarctica, *Nat. Geosci.*, 8, 294–298,
717 <https://doi.org/10.1038/ngeo2388>, 2015.

718 Haeger, C., Petrunin, A. G., and Kaban, M. K.: Geothermal Heat Flow and Thermal Structure of the
719 Antarctic Lithosphere, *Geochem. Geophys. Geosystems*, 23, e2022GC010501,
720 <https://doi.org/10.1029/2022GC010501>, 2022.

721 Huang, Y., Zhao, L., Wolovick, M., Ma, Y., and Moore, J. C.: Using specularity content to evaluate
722 eight geothermal heat flow maps of Totten Glacier, *The Cryosphere*, 18, 103–119,
723 <https://doi.org/10.5194/tc-18-103-2024>, 2024.

724 Jordan, T. M., Martín, C., Brisbourne, A. M., Schroeder, D. M., and Smith, A. M.: Radar
725 Characterization of Ice Crystal Orientation Fabric and Anisotropic Viscosity Within an
726 Antarctic Ice Stream, *J. Geophys. Res. Earth Surf.*, 127, e2022JF006673,
727 <https://doi.org/10.1029/2022JF006673>, 2022.

728 Kamb, B.: Sliding motion of glaciers: Theory and observation, *Rev. Geophys.*, 8, 673–728,
729 <https://doi.org/10.1029/RG008i004p00673>, 1970.

730 Kang, H., Zhao, L., Wolovick, M., and Moore, J. C.: Evaluation of six geothermal heat flux maps
731 for the Antarctic Lambert–Amery glacial system, *The Cryosphere*, 16, 3619–3633,
732 <https://doi.org/10.5194/tc-16-3619-2022>, 2022.

733 Kim, B.-H., Seo, K.-W., Lee, C.-K., Kim, J.-S., Lee, W. S., Jin, E. K., and Van Den Broeke, M.:
734 Partitioning the drivers of Antarctic glacier mass balance (2003–2020) using satellite
735 observations and a regional climate model, *Proc. Natl. Acad. Sci.*, 121, e2322622121,
736 <https://doi.org/10.1073/pnas.2322622121>, 2024.

737 Larour, E., Seroussi, H., Morlighem, M., and Rignot, E.: Continental scale, high order, high spatial
738 resolution, ice sheet modeling using the Ice Sheet System Model (ISSM), *J. Geophys. Res.*,
739 117, F01022, <https://doi.org/10.1029/2011JF002140>, 2012.

740 Le Brocq, A. M., Payne, A. J., and Vieli, A.: An improved Antarctic dataset for high resolution
741 numerical ice sheet models (ALBMAP v1), *Earth Syst. Sci. Data*, 2, 247–260,
742 <https://doi.org/10.5194/essd-2-247-2010>, 2010.

743 Lipscomb, W. H., Leguy, G. R., Jourdain, N. C., Asay-Davis, X., Seroussi, H., and Nowicki, S.:
744 ISMIP6-based projections of ocean-forced Antarctic Ice Sheet evolution using the
745 Community Ice Sheet Model, *The Cryosphere*, 15, 633–661, [https://doi.org/10.5194/tc-15-](https://doi.org/10.5194/tc-15-633-2021)
746 633-2021, 2021.

747 Lhermitte, S., Sun, S., Shuman, C., Wouters, B., Pattyn, F., Wuite, J., Berthier, E., and Nagler, T.:
748 Damage accelerates ice shelf instability and mass loss in Amundsen Sea Embayment, *Proc.*
749 *Natl. Acad. Sci.*, 117, 24735–24741, <https://doi.org/10.1073/pnas.1912890117>, 2020.

750 Lösing, M. and Ebbing, J.: Predicting Geothermal Heat Flow in Antarctica With a Machine Learning
751 Approach, *J. Geophys. Res. Solid Earth*, 126, e2020JB021499,
752 <https://doi.org/10.1029/2020JB021499>, 2021.

753 MacAyeal, D. R.: A tutorial on the use of control methods in ice-sheet modeling, *J. Glaciol.*, 39, 91–
754 98, <https://doi.org/10.3189/S0022143000015744>, 1993.

755 Martín, C., Gudmundsson, G. H., Pritchard, H. D., and Gagliardini, O.: On the effects of anisotropic
756 rheology on ice flow, internal structure, and the age-depth relationship at ice divides, *J.*
757 *Geophys. Res. Earth Surf.*, 114, F04001, <https://doi.org/10.1029/2008JF001204>, 2009.

758 Martos, Y. M., Catalán, M., Jordan, T. A., Golynsky, A., Golynsky, D., Eagles, G., and Vaughan, D.
759 G.: Heat Flux Distribution of Antarctica Unveiled, *Geophys. Res. Lett.*, 44, 11,417–11,426,
760 <https://doi.org/10.1002/2017GL075609>, 2017.

761 Maule, C. F., Purucker, M. E., Olsen, N., and Mosegaard, K.: Heat Flux Anomalies in Antarctica
762 Revealed by Satellite Magnetic Data, *Science*, 309, 464–467,
763 <https://doi.org/10.1126/science.1106888>, 2005.

764 McCormack, F. S., Roberts, J. L., Dow, C. F., Stål, T., Halpin, J. A., Reading, A. M., and Siegert, M.
765 J.: Fine-Scale Geothermal Heat Flow in Antarctica Can Increase Simulated Subglacial Melt
766 Estimates, *Geophys. Res. Lett.*, 49, e2022GL098539, <https://doi.org/10.1029/2022GL098539>,
767 2022.

768 Morlighem, M., Seroussi, H., Larour, E., and Rignot, E.: Inversion of basal friction in Antarctica
769 using exact and incomplete adjoints of a higher-order model, *J. Geophys. Res. Earth Surf.*, 118,
770 1746–1753, <https://doi.org/10.1002/jgrf.20125>, 2013.

771 Morlighem, M., Rignot, E., Binder, T., Blankenship, D., Drews, R., Eagles, G., Eisen, O., Ferraccioli,
772 F., Forsberg, R., Fretwell, P., Goel, V., Greenbaum, J. S., Gudmundsson, H., Guo, J., Helm, V.,
773 Hofstede, C., Howat, I., Humbert, A., Jokat, W., Karlsson, N. B., Lee, W. S., Matsuoka, K.,
774 Millan, R., Mouginot, J., Paden, J., Pattyn, F., Roberts, J., Rosier, S., Ruppel, A., Seroussi, H.,
775 Smith, E. C., Steinhage, D., Sun, B., Broeke, M. R. V. D., Ommen, T. D. V., Wessem, M. V.,
776 and Young, D. A.: Deep glacial troughs and stabilizing ridges unveiled beneath the margins of
777 the Antarctic ice sheet, *Nat. Geosci.*, 13, 132–137, [https://doi.org/10.1038/s41561-019-0510-](https://doi.org/10.1038/s41561-019-0510-8)
778 8, 2020.

779 Nye, J. F.: Glacier sliding without cavitation in a linear viscous approximation, *Proc. R. Soc. Lond.*
780 *Math. Phys. Sci.*, 315, 381–403, <https://doi.org/10.1098/rspa.1970.0050>, 1970.

781 Park, I.-W., Jin, E. K., Morlighem, M., and Lee, K.-K.: Impact of boundary conditions on the
782 modeled thermal regime of the Antarctic ice sheet, *The Cryosphere*, 18, 1139–1155,
783 <https://doi.org/10.5194/tc-18-1139-2024>, 2024.

784 Paterson, W. S. B.: Why ice-age ice is sometimes “soft,” *Cold Reg. Sci. Technol.*, 20, 75–98,
785 [https://doi.org/10.1016/0165-232X\(91\)90058-O](https://doi.org/10.1016/0165-232X(91)90058-O), 1991.

786 Pattyn, F.: Sea-level response to melting of Antarctic ice shelves on multi-centennial timescales
787 with the fast Elementary Thermomechanical Ice Sheet model (f.ETISh v1.0), *The*
788 *Cryosphere*, 11, 1851–1878, <https://doi.org/10.5194/tc-11-1851-2017>, 2017.

789 Payne, A. J., Nowicki, S., Abe-Ouchi, A., Agosta, C., Alexander, P., Albrecht, T., Asay-Davis, X.,
790 Aschwanden, A., Barthel, A., Bracegirdle, T. J., Calov, R., Chambers, C., Choi, Y., Cullather,
791 R., Cuzzone, J., Dumas, C., Edwards, T. L., Felikson, D., Fettweis, X., Galton-Fenzi, B. K.,
792 Goelzer, H., Gladstone, R., Golledge, N. R., Gregory, J. M., Greve, R., Hattermann, T.,
793 Hoffman, M. J., Humbert, A., Huybrechts, P., Jourdain, N. C., Kleiner, T., Munneke, P. K.,
794 Larour, E., Le Clec’H, S., Lee, V., Leguy, G., Lipscomb, W. H., Little, C. M., Lowry, D. P.,
795 Morlighem, M., Nias, I., Pattyn, F., Pelle, T., Price, S. F., Quiquet, A., Reese, R., Rückamp, M.,
796 Schlegel, N., Seroussi, H., Shepherd, A., Simon, E., Slater, D., Smith, R. S., Straneo, F., Sun,
797 S., Tarasov, L., Trusel, L. D., Van Breedam, J., Van De Wal, R., Van Den Broeke, M.,
798 Winkelmann, R., Zhao, C., Zhang, T., and Zwinger, T.: Future Sea Level Change Under
799 Coupled Model Intercomparison Project Phase 5 and Phase 6 Scenarios From the Greenland
800 and Antarctic Ice Sheets, *Geophys. Res. Lett.*, 48, e2020GL091741,

801 <https://doi.org/10.1029/2020GL091741>, 2021.

802 Peyaud, V., Bouchayer, C., Gagliardini, O., Vincent, C., Gillet-Chaulet, F., Six, D., and Laarman,
803 O.: Numerical modeling of the dynamics of the Mer de Glace glacier, French Alps: comparison
804 with past observations and forecasting of near-future evolution, *The Cryosphere*, 14, 3979–
805 3994, <https://doi.org/10.5194/tc-14-3979-2020>, 2020.

806 Pittard, M. L., Roberts, J. L., Galton-Fenzi, B. K., and Watson, C. S.: Sensitivity of the Lambert-
807 Amery glacial system to geothermal heat flux, *Ann. Glaciol.*, 57, 56 – 68,
808 <https://doi.org/10.1017/aog.2016.26>, 2016.

809 Pollard, D. and DeConto, R. M.: A simple inverse method for the distribution of basal sliding
810 coefficients under ice sheets, applied to Antarctica, *The Cryosphere*, 6, 953–971,
811 <https://doi.org/10.5194/tc-6-953-2012>, 2012.

812 Pritchard, H. D., Arthern, R. J., Vaughan, D. G., and Edwards, L. A.: Extensive dynamic thinning
813 on the margins of the Greenland and Antarctic ice sheets, *Nature*, 461, 971–975,
814 <https://doi.org/10.1038/nature08471>, 2009.

815 Pritchard, H.D., Fretwell, P.T., Fremant, A.C. et al. Bedmap3 updated ice bed, surface and thickness
816 gridded datasets for Antarctica. *Sci Data* 12, 414 (2025). [https://doi.org/10.1038/s41597-025-](https://doi.org/10.1038/s41597-025-04672-y)
817 [04672-y](https://doi.org/10.1038/s41597-025-04672-y)

818 Purucker, M.: Geothermal heat flux data set based on low resolution observations collected by the
819 CHAMP satellite between 2000 and 2010, and produced from the MF-6 model following the
820 technique described in Fox Maule et al. (2005), Interactive System for Ice sheet Simulation
821 [data set], https://core2.gsfc.nasa.gov/research/purucker/heatflux_mf7_foxmaule05.txt (last
822 access: 24 December 2023), 2012.

823 Rathmann, N. M. and Lilien, D. A.: Inferred basal friction and mass flux affected by crystal-
824 orientation fabrics, *J. Glaciol.*, 68, 236–252, <https://doi.org/10.1017/jog.2021.88>, 2022.

825 Reading, A. M.: Antarctic geothermal heat flow and its implications for tectonics and ice sheets,
826 *Nat. Rev. Earth Environ.*, 3, 814–831, <https://doi.org/10.1038/s43017-022-00348-y>, 2022.

827 Reese, R., Garbe, J., Hill, E. A., Urruty, B., Naughten, K. A., Gagliardini, O., Durand, G., Gillet-
828 Chaulet, F., Gudmundsson, G. H., Chandler, D., Langebroek, P. M., and Winkelmann, R.: The
829 stability of present-day Antarctic grounding lines – Part 2: Onset of irreversible retreat of
830 Amundsen Sea glaciers under current climate on centennial timescales cannot be excluded,
831 *The Cryosphere*, 17, 3761–3783, <https://doi.org/10.5194/tc-17-3761-2023>, 2023.

832 Ross, N., Bingham, R. G., Corr, H. F. J., Ferraccioli, F., Jordan, T. A., Le Brocq, A., Rippin, D. M.,
833 Young, D., Blankenship, D. D., and Siegert, M. J.: Steep reverse bed slope at the grounding
834 line of the Weddell Sea sector in West Antarctica, *Nat. Geosci.*, 5, 393–396,
835 <https://doi.org/10.1038/ngeo1468>, 2012.

836 Rignot, E., Mouginot, J., and Scheuchl, B.: MEaSURES InSAR-Based Antarctica Ice Velocity Map,
837 Version 2, Boulder, Colorado USA, NASA National Snow and Ice Data Center Distributed
838 Active Archive Center [data Set], <https://doi.org/10.5067/D7GK8F5J8M8R>, 2017.

839 Rignot, E., Mouginot, J., Scheuchl, B., Van Den Broeke, M., Van Wessel, M. J., and Morlighem,
840 M.: Four decades of Antarctic Ice Sheet mass balance from 1979–2017, *Proc. Natl. Acad. Sci.*,

841 116, 1095–1103, <https://doi.org/10.1073/pnas.1812883116>, 2019.

842 Schannwell, C., Drews, R., Ehlers, T. A., Eisen, O., Mayer, C., Malinen, M., Smith, E. C., and
843 Eisermann, H.: Quantifying the effect of ocean bed properties on ice sheet geometry over 40
844 000 years with a full-Stokes model, *The Cryosphere*, 14, 3917–3934,
845 <https://doi.org/10.5194/tc-14-3917-2020>, 2020.

846 Schoof, C.: On the mechanics of ice-stream shear margins, *J. Glaciol.*, 50, 208–218,
847 <https://doi.org/10.3189/172756504781830024>, 2004.

848 Schoof, C.: The effect of cavitation on glacier sliding, *Proc. R. Soc. Math. Phys. Eng. Sci.*, 461,
849 609–627, <https://doi.org/10.1098/rspa.2004.1350>, 2005.

850 Schroeder, D. M., Blankenship, D. D., and Young, D. A.: Evidence for a water system transition
851 beneath Thwaites Glacier, West Antarctica, *Proc. Natl. Acad. Sci.*, 110, 12225–12228,
852 <https://doi.org/10.1073/pnas.1302828110>, 2013.

853 Schroeder, D. M., Blankenship, D. D., Raney, R. K., and Grima, C.: Estimating Subglacial Water
854 Geometry Using Radar Bed Echo Specularity: Application to Thwaites Glacier, West
855 Antarctica, *IEEE Geosci. Remote Sens. Lett.*, 12, 443–447,
856 <https://doi.org/10.1109/LGRS.2014.2337878>, 2015.

857 Seroussi, H., Nowicki, S., Simon, E., Abe-Ouchi, A., Albrecht, T., Brondex, J., Cornford, S., Dumas,
858 C., Gillet-Chaulet, F., Goelzer, H., Gолledge, N. R., Gregory, J. M., Greve, R., Hoffman, M. J.,
859 Humbert, A., Huybrechts, P., Kleiner, T., Larour, E., Leguy, G., Lipscomb, W. H., Lowry, D.,
860 Mengel, M., Morlighem, M., Pattyn, F., Payne, A. J., Pollard, D., Price, S. F., Quiquet, A.,
861 Reerink, T. J., Reese, R., Rodehacke, C. B., Schlegel, N.-J., Shepherd, A., Sun, S., Sutter, J.,
862 Van Breedam, J., Van De Wal, R. S. W., Winkelmann, R., and Zhang, T.: initMIP-Antarctica:
863 an ice sheet model initialization experiment of ISMIP6, *The Cryosphere*, 13, 1441–1471,
864 <https://doi.org/10.5194/tc-13-1441-2019>, 2019.

865 Shackleton, C., Matsuoka, K., Moholdt, G., Van Liefferinge, B., and Paden, J.: Stochastic
866 Simulations of Bed Topography Constrain Geothermal Heat Flow and Subglacial Drainage
867 Near Dome Fuji, East Antarctica, *J. Geophys. Res. Earth Surf.*, 128, e2023JF007269,
868 <https://doi.org/10.1029/2023JF007269>, 2023.

869 Shapiro, N.: Inferring surface heat flux distributions guided by a global seismic model: particular
870 application to Antarctica, *Earth Planet. Sci. Lett.*, 223, 213–224,
871 <https://doi.org/10.1016/j.epsl.2004.04.011>, 2004.

872 Shen, W., Wiens, D. A., Lloyd, A. J., and Nyblade, A. A.: A Geothermal Heat Flux Map of Antarctica
873 Empirically Constrained by Seismic Structure, *Geophys. Res. Lett.*, 47, e2020GL086955,
874 <https://doi.org/10.1029/2020GL086955>, 2020.

875 Siahann, A., Smith, R. S., Holland, P. R., Jenkins, A., Gregory, J. M., Lee, V., Mathiot, P., Payne, A.
876 J., Ridley, J. K., and Jones, C. G.: The Antarctic contribution to 21st-century sea-level rise
877 predicted by the UK Earth System Model with an interactive ice sheet, *The Cryosphere*, 16,
878 4053 – 4086, <https://doi.org/10.5194/tc-16-4053-2022>, 2022.

879 Smith-Johnsen, S., Schlegel, N. -J., De Fleurian, B., and Nisancioglu, K. H.: Sensitivity of the
880 Northeast Greenland Ice Stream to Geothermal Heat, *J. Geophys. Res. Earth Surf.*, 125,

881 e2019JF005252, <https://doi.org/10.1029/2019JF005252>, 2020.

882 Stål, T., Reading, A. M., Halpin, J. A., and Whittaker, J. M.: Antarctic Geothermal Heat Flow Model:
883 Aq1, *Geochem. Geophys. Geosystems*, 22, e2020GC009428,
884 <https://doi.org/10.1029/2020GC009428>, 2021.

885 Sun, S., Cornford, S. L., Moore, J. C., Gladstone, R., and Zhao, L.: Ice shelf fracture
886 parameterization in an ice sheet model, *The Cryosphere*, 11, 2543–2554,
887 <https://doi.org/10.5194/tc-11-2543-2017>, 2017.

888 Tsai, V. C., Stewart, A. L., and Thompson, A. F.: Marine ice-sheet profiles and stability under
889 Coulomb basal conditions, *J. Glaciol.*, 61, 205–215, <https://doi.org/10.3189/2015JoG14J221>,
890 2015.

891 Van Liefferinge, B., Pattyn, F., Cavitte, M. G. P., Karlsson, N. B., Young, D. A., Sutter, J., and Eisen,
892 O.: Promising Oldest Ice sites in East Antarctica based on thermodynamical modelling, *The*
893 *Cryosphere*, 12, 2773–2787, <https://doi.org/10.5194/tc-12-2773-2018>, 2018.

894 Weertman, J.: On the Sliding of Glaciers, *J. Glaciol.*, 3, 33–38,
895 <https://doi.org/10.3189/S0022143000024709>, 1957.

896 Young, D. A., Schroeder, D. M., Blankenship, D. D., Kempf, S. D., and Quartini, E.: The distribution
897 of basal water between Antarctic subglacial lakes from radar sounding, *Philos. Trans. R. Soc.*
898 *Math. Phys. Eng. Sci.*, 374, 20140297, <https://doi.org/10.1098/rsta.2014.0297>, 2016.

899 Zhao, C., Gladstone, R. M., Warner, R. C., King, M. A., Zwinger, T., and Morlighem, M.: Basal
900 friction of Fleming Glacier, Antarctica – Part 1: Sensitivity of inversion to temperature and
901 bedrock uncertainty, *The Cryosphere*, 12, 2637–2652, [https://doi.org/10.5194/tc-12-2637-](https://doi.org/10.5194/tc-12-2637-2018)
902 2018, 2018a.

903 Zhao, L., Moore, J. C., Sun, B., Tang, X., and Guo, X.: Where is the 1-million-year-old ice at Dome
904 A?, *The Cryosphere*, 12, 1651–1663, <https://doi.org/10.5194/tc-12-1651-2018>, 2018b.

905 Zhang, X., Dong, X., Zeng, J., Hou, S., Smeets, P., Reijmer, C. H., and Wang, Y., Spatiotemporal
906 Reconstruction of Antarctic Near-Surface Air Temperature from MODIS Observations, *J.*
907 *Clim.*, 35, 5537–5553, 2022.

908 Zwinger, T., Schäfer, M., Martín, C., and Moore, J. C.: Influence of anisotropy on velocity and age
909 distribution at Scharffenbergbotnen blue ice area, *The Cryosphere*, 8, 607–621,
910 <https://doi.org/10.5194/tc-8-607-2014>, 2014.

911